A novel method for the measurement of flotation recovery by means of 4D particle tracking velocimetry

Sommer, A.-E.; Nikpay, M.; Heitkam, S.; Rudolph, M.; Eckert, K.;

Originally published:

May 2018

Minerals Engineering 124(2018), 116-122

DOI: https://doi.org/10.1016/j.mineng.2018.05.006

Perma-Link to Publication Repository of HZDR:

https://www.hzdr.de/publications/Publ-26749

A novel method for the measurement of flotation recovery by means of 4D particle tracking velocimetry

A.-E. Sommer[a,*], M. Nikpay[a], S. Heitkam[b], M. Rudolph[c], K. Eckert[a,b]

[a] *Helmholtz-Zentrum Dresden-Rossendorf, Institute of Fluid Dynamics, Bautzner Landstrasse 400, 01328 Dresden, Germany*
[b] *Technische Universität Dresden, Institute of Process Engineering and Environmental Technology, Helmholtzstrasse 14, 01062 Dresden, Germany*
[c] *Helmholtz-Zentrum Dresden-Rossendorf, Helmholtz Institute Freiberg for Resource Technology, Chemnitzer Strasse 40, 09599 Freiberg, Germany*

Abstract

This work focuses on the analysis of the collection process in flotation by a simultaneous time-resolved measurement of particle and bubble trajectories. We introduced a new method that determined the probability of collision and attachment by a 3D particle tracking method with high temporal (1000 fps) and spatial (0.03 mm/pixel) resolution in the dense particle flow (5000 particles/ml). A tomographic particle image velocimetry device with three high-speed cameras recorded the three-phase flow in a rectangular bubble column (bubble chain). Particles made of fluorescent polystyrene were employed so that particles appeared bright and bubbles dark on the captured images. An attachment occurred if the trajectory of a particle coincided with that of a bubble. The recovery was calculated based on the number of particles attached to a bubble compared to the total particles density. With this method, the true flotation depending on the particle diameter ($30 - 100$ μm) was investigated and compared the results with an existing model of the bubble-particle collection microprocess.

Keywords: Collection zone recovery, Particle tracking velocimetry, Polystyrene flotation, Bubble-particle interaction

1. Introduction

Froth flotation is the most important and widely used process for the separation of valuable minerals e.g. copper sulfides, galena or scheelite from the gangue within the ores. Billions of tons of ore are treated annually by flotation in the mining industry. The efficiency of the froth flotation process depends on the interaction of hydrophobized particles and bubbles, controlled by both the surface chemistry and the hydrodynamics in the pulp. Flotation covers a wide range of length scales from the nano-scale of rupturing liquid films between bubbles and particles towards the macro-scale of flow structures within a flotation cell. In order to simulate such systems, sufficient models for the small-scale effects have to be developed.

The rate of removal of the target particles in batchwise flotation is described frequently by a first-order rate equation with a kinetic constant k. Ultimate goal is to predict the flotation rate constant for minerals from first principles (e.g. Nguyen and Schulze, 2003; Ralston et al., 1999; Sutherland, 1948; Yoon, 2000; Yoon et al., 2016).

For that purpose, the particle collection process in the pulp is divided into a sequence of elementary sub-process, namely collision, attachment, and detachment which are represented by probabilities P_i or efficiencies E_i. These probabilities are modeled in terms of physicochemical and geometrical parameters (e.g. Sharma and Ruckenstein, 1990; Yoon and Luttrell, 1989), such as contact angle, particle size, and the Reynolds number of bubbles (Schubert, 1999).

*Corresponding author
Email address: a.sommer@hzdr.de (A.-E. Sommer)

Thus, a direct way to measure the recovery at defined hydrodynamic conditions would be very helpful to verify these models and to advance our understanding of particular microprocesses. To do so, this work presents a new approach to measure the collection in the pulp zone in flotation. It is based on an optical 3D particle tracking velocimetry (PTV) with a high temporal resolution, a so called 4D PTV, which is used to identify particle trajectories and attached particles on bubbles. In contrast to other methods, based e.g. on a sampling tube inserted below the pulp interface to collect loaded bubbles (Anfruns and Kitchener, 1977; Falutsu and Dobby, 1989; Hewitt et al., 1995; Moys et al., 2010; Seaman et al., 2004), this method is completely non-invasive. The former PTV was restricted to a low particle seeding density (0.005 particles per pixel (Schanz et al., 2016)). Recent developments in this field enabled the application of PTV to flows with 20 times higher particle densities (up to 0.1 particles per pixel) which is more close to the conditions in the pulp zone of a flotation cell. Milestones were a time-resolved tomographic particle image velocimetry (tomo PIV) (Scarano, 2012) and advanced tracking algorithms as the Shake-the-box algorithm from Schanz et al. (2016).

Based on the recorded images, we developed a method to identify attached particles. A bubble mask was generated to separate the bubble and particle image. The tracks for each phase were calculated individually with the algorithm of Schanz et al. (2016) and Maas (1996). The attached particles were located based on their relative position to the bubble surface and their radial velocity. Subsequently, the collection zone recovery was calculated as a ratio of attached particle per bubble to all particles within a reference volume based on the rising path of a bubble. Finally, this method was applied to investigate the collection in the pulp zone depending on particle diameter. The results are compared with the model from Nguyen et al. (1998).

2. Experimental setup

2.1. Bubble column

To generate a simple model flow in order to prove our method, the experimental setup of a bubble column was adapted from Ziegenhein and Lucas (2016). A bubble chain rose up in a rectangular column with an inner size of 90×25 mm^2 and a water level of 200 mm (Fig. 4). The gas was dispersed 65 mm above the ground plate by a needle with an inner diameter of 0.3 mm. The produced bubble diameter was adjusted to 2.3 ± 0.1 mm (see section 2.2) by setting a gas flow of 0.02 l/min. The particle and bubble trajectories were measured at the gas outlet in a volume of $37 \times 23 \times 5$ mm^3 along the center.

2.2. Polystyrene particles and reagents

Polystyrene (PS) particles (microparticles GmbH Berlin) with an incorporated fluorescent dye (red-fluorescent: Ex/Em 530 nm/607 nm) were used as model particles. The diameter of the particles was varied between 33.03 μm and 95.07 μm. Different strategies exists in the literature to ensure flotability of PS particles (Fraunholcz, 1997; Pascoe, 2005; Wang et al., 2016). In this work, a nontoxic surfactant, Poly(ethylene glycol)-*block*-poly(propylene glycol)-*block*-poly(ethylene glycol) (PEG-PPG-PEG), see Fig. 1, was used. PEG-PPG-PEG is a nonionic surfactant with a hydrophilic-lipophilic balance (HLB) number between 7 and 9. A stock solution with a PEG-PPG-PEG concentration of 20 g/l in deionized water was prepared into which the PS particles with a concentration of 7.3 g/l were added for 24 hours. For the experiments the bubble column was filled with deionized water, potassium chloride KCl (10 mM) and the PS particles conditioned as described above. The flotatability of the PS particles was proved by a microscopic inspection of the froth formed by increasing the gas flow rate up to 0.5 l/min. Fig. 2 shows clearly the attachment of PS particles in the froth.

When changing the particle diameter, a higher mass fraction of PS was added. Tab. 1 summarizes the composition of the liquid and solid phases. Since an increase in the mass fraction of PS is coupled with a small increase of the concentration of PEG-PPG-PEG, the surface tension drops. As a result, also the sauter diameter of the bubble ($d_{32} = \frac{\sum_i d_{b,i}^3}{\sum_i d_{b,i}^2}$) decreases as shown in Fig. 3.

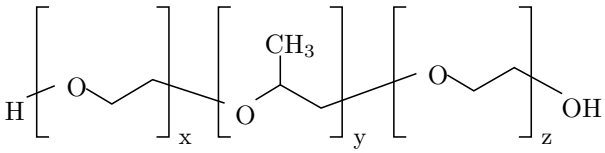

Figure 1: Structural formula of the non-ionic surfactant Poly(ethylene glycol)-*block*-poly(propylene glycol)-*block*-poly(ethylene glycol) (PEG-PPG-PEG).

	PS33	PS48	PS95
d_p in μm	33.03	48.2	95.07
c_{PS} in g/l	0.15	0.22	0.37
c_s in g/l	0.4	0.6	1.0
σ in mN/m	30.7	29.7	27.8

Table 1: Properties of the solid (particle diameter d_p and concentration of polystyrene c_{PS} for the three different types of particles) and liquid phase (concentration of PEG-PPG-PEG c_s and surface tension σ). The density of all PS particles was $\rho_{PS} = 1.2$ g/l. The KCl concentration was 10 mM.

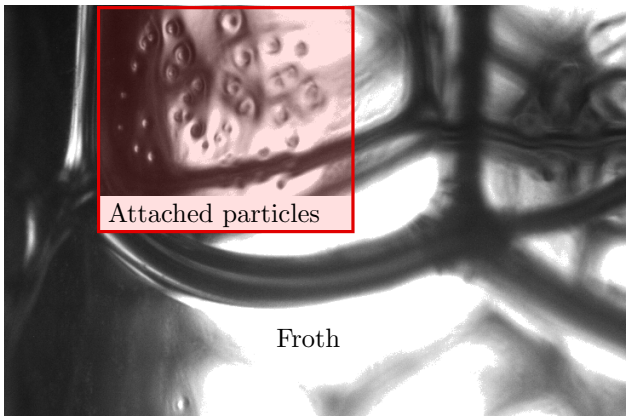

Figure 2: Image of froth with PS particles to prove the flotability in the current setup.

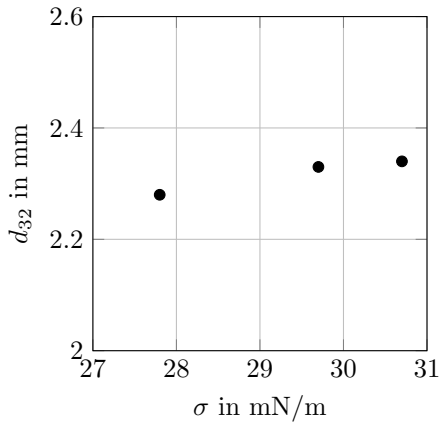

Figure 3: Dependence of sauter mean diameter d_{32} on the surface tension σ.

Illumination	Intensity	62 W
	λ	527 nm
	Measurement volume thickness	5 mm
Recording	Resolution	1280 px x 800 px
	Spatial resolution	0.03 mm/px
	Frame rate	1000 fps
	Exposure time	1000 μs
	Field of view	37 mm x 23 mm
	Image depth	8 Bit

Table 2: Properties and parameters of the tomo PIV setup.

3. 4D Particle tracking velocimetry

3.1. Measurement device

For the PTV measurement, we used a tomo PIV system(LaVision, Göttingen, Germany), see Fig. 4). Tomo PIV is an optical 3D measurement technique to measure the velocity of a fluid flow represented by tracer particles. Sufficiently small and neutrally buoyant particles follow the streamlines of the fluid flow with negligible deviation. Thus, the fluid velocity is assumed as equal to the particle velocity. The particles are illuminated by a laser and scatter its light. The scattered light is captured by at least three cameras from different viewing angles.

The difference between tomo PIV and PTV lies in the subsequent data evaluation. In traditional tomo PIV a 3D3C velocity field is calculated by statistical methods as cross-correlation (Scarano, 2012). Conversely, in PTV the position of each particle is triangulated to gain the Lagrangian particle trajectory field (Schanz et al., 2016). Consequently, the influence of a bubble on the trajectory of individual particles can be observed.

For our application, we adopted this technique as follows (Tab. 2). Three high-speed cameras in a linear imaging configuration observed the measurement volume illuminated by a Nd-YLF laser. The fluorescent PS particles absorbed the laser light and emitted light with a wavelength λ_{em} of 607 nm.

Fluorescent particles as seeding particles were used for bubble flows by various research groups (e.g. Lindken and Merzkirch, 2002; Ziegenhein and Lucas, 2016). An optical longpass filter was applied to the camera objectives to block the laser light, so that only the light emitted by the fluorescent seeding particles was recorded. Thus, the scattered laser light from the bubbles was blocked. However, the bubbles also reflected the fluorescent light at much lower intensity which enabled a simultaneous recording of bubbles and particles. The separation of these two signals is described in detail in section 3.2.

Before each measurement, a spatial calibration was carried out. For a successful particle triangulation with the Shake-the-Box algorithm, a calibration error lower than a fraction of the particle image diameter (Elsinga et al., 2006) was required. Therefore, the mapping function was not only calculated through an image of a two plane calibration plate (50 mm x 50 mm, No. 058-5 from LaVision) but also the volume self-calibration procedure from Wieneke (2008) was applied. To that end, a set of images with a lower seeding density and no air bubbles were recorded. The 3D position of each particle was computed by triangulation of matching particles. The residual triangulation error was then used to correct the mapping functions for all cameras. This procedure detected large misalignment errors (up to several pixels) and reduced them to below 0.1 px in the entire measurement volume which was necessary for a successful triangulation.

3.2. Image processing

For the calculation of the collection zone recovery R_c, the data analysis of the recorded image was divided into two subprocesses. Firstly, the bubble and particle trajectories were computed. Hereby, an image processing algorithm was applied to compute a bubble mask. Secondly, the attached particles were detected in order to calculate R_c which is described in section 3.4.

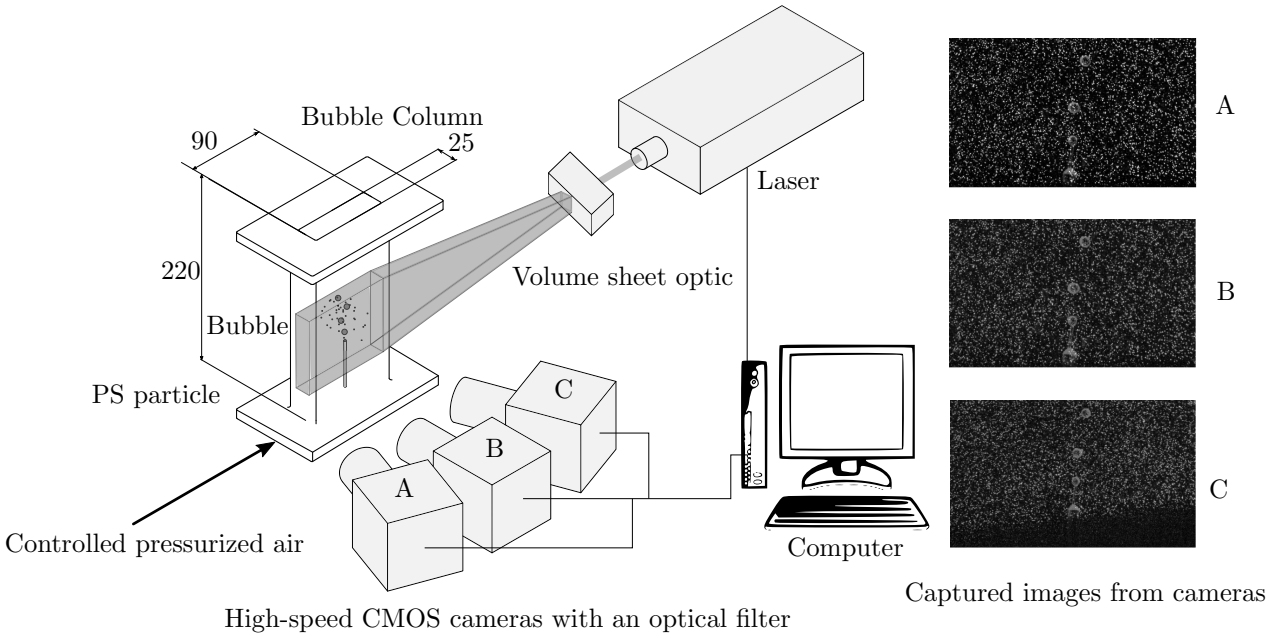

Figure 4: Experimental setup of the tomo PIV system to measure the particle attachment in a bubble column.

The image processing algorithm for masking out the bubbles was inspired by Lindken and Merzkirch (2002) which distinguishes the bubbles and particles by their intensity level. By the usage of the optical longpass filter during the experiments, the particles appeared brighter than the bubbles within the captured image (Fig. 5a). Therefore, a Gaussian and a median filter (3×3 px^2) was applied to blur the high-intensity values of the particles. The image contrast was enhanced by an equalization of the histogram of the image. Subsequently, the bubbles were the brightest objects within the image (Fig. 5b). In the next step, a circular Hough transformation (Atherton and Kerbyson, 1999; Yuen et al., 1989) was used to recognize the 2D bubble image as a circular object (Fig. 5c). The detected bubbles were cut out and segmented individually. This was possible because bubbles in the bubble chain remained well separated.

For the binarization, an adaptive gray value threshold was applied (Fig. 5d). The threshold value for each individual bubble was calculated based on the mean gray value between the boundaries of the bubble. In the recorded images, a bubble appeared as a bright circular ring with a dark circle in the middle (Fig. 6a). Consequently, the boundaries of a bubble were defined by the highest gradient before or respectively after the highest gray value (Fig. 6b). Finally, the non-detected bubble areas were filled up yielding to the bubble mask (Fig. 5e).

3.3. Trajectory calculation

In the next step, the trajectories were calculated separately for each phase. The particle trajectories were triangulated with the Shake-the-box algorithm supplied by LaVision's software DaVis 8.4. This algorithm computes the Lagrangian tracks of particles through a prediction of the particle trajectory based on preceding time steps. Uncertainties between predicted and existing position are corrected by a variation of the predicted position in space ('shaking') till it matches the existing position. Newly entered particles are triangulated by an iterative reconstruction (Wieneke, 2012). A more detailed description of this algorithm can be found in Schanz et al. (2016). The Shake-the-box algorithm was applied to the captured tomo PIV images. To avoid errors caused by the recorded bubbles in these images, the bubble mask multiplied by the maximum bubble intensity were subtracted from the captured image (Fig. 7a). Consequently, particles located in front of the bubble remained in the image, if their image intensity was higher than the one from the bubble. The particle tracks are illustrated for ten time steps in Fig. 7b.

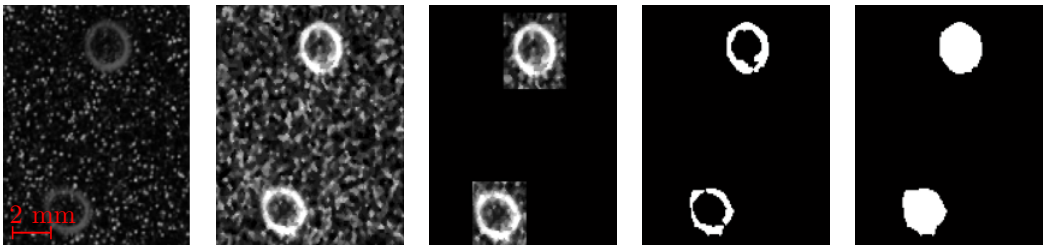

Figure 5: Image processing steps to define a mask for bubbles in the captured images. (a) Original image. (b) Image preprocessing to blur particles by a Gaussian and a median filter and enhance bubble contrast by a histogram equalization. (c) Cropped bubble image after Hough transformation. (d) Binarization with adaptive gray value threshold. (e) Image of bubble mask after filling up non-detected bubble areas.

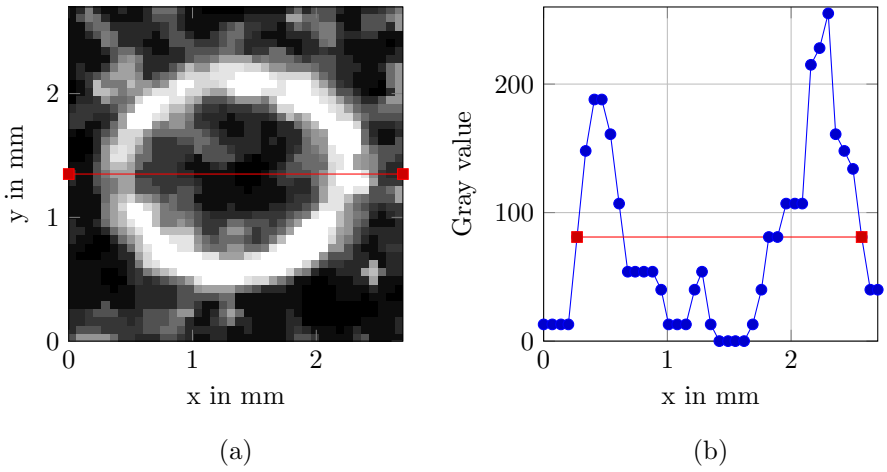

Figure 6: Calculation of the adaptive gray value threshold. (a) Appearance of the bubble in the image with a bright circular ring and a dark circle in the middle. (b) Corresponding gray values along the middle axis of a bubble (illustrated as red line in (a)). The computed threshold value is illustrated as red squares.

	PS33	PS48	PS95
Eo	1.7	1.6	1.5
Re	484	484	484

Table 3: Eötvös Eo and Reynolds number Re of the bubbles during the measurements with different PS particles.

Simultaneously, the bubble trajectories were determined using a 3D PTV algorithm from Maas et al. (1993) in LaVision's software DaVis 8.4. The lower number of tracked objects allowed for the application of a general and less demanding algorithm. The PTV algorithm from Maas et al. (1993) was applied to the midpoints of the bubble (Fig. 7c).

Both algorithm provided results in the form of a trajectory. The trajectory consisted of the respective position $\boldsymbol{X_j}$ which is a tuple of the three coordinates (x_j, y_j, z_j) and the corresponding velocity vector $\boldsymbol{V_j}$ with its three velocity component in each direction in space (u_j, v_j, w_j). For further explanations the following notation is used

- Points and Vectors: capital letters in bold e.g. $\boldsymbol{X_b}$, $\boldsymbol{V_b}$
- Coordinates, velocity components for each direction in space: small letters e.g. x_b, u_p.

Thereof, the particle and bubble trajectories are described with these variables

$$\text{Particle}: \boldsymbol{X_p} = (x_p, y_p, z_p)^T,\ \boldsymbol{V_p} = (u_p, v_p, w_p)^T$$
$$\text{Bubble}: \boldsymbol{X_b} = (x_b, y_b, z_b)^T,\ \boldsymbol{V_b} = (u_b, v_b, w_b)^T.$$

To quantify the interaction between particles and bubbles, the shape of each object was approximated and their trajectories were combined again. Particles were described as points whereas the bubble shape was approximated as an oblate spheroid (Fig. 8). This approximation bases on Grace's bubble shape prediction diagramm (Clift et al., 2005) taking the Eötvös Eo and Reynolds number Re into account

$$Eo = \frac{\rho_l g d_b^2}{\sigma} \tag{1}$$

$$Re = \frac{|\boldsymbol{V_b}| d_b \rho_l}{\eta_l}. \tag{2}$$

with ρ_l the liquid density, g the gravitational acceleration, d_b the volume equivalent bubble diameter ($d_b = \sqrt[3]{8a^2c}$), σ the surface tension, $|\boldsymbol{V_b}|$ the rising velocity of a bubble and η_l the dynamic viscosity. For the range displayed in Tab. 3, Clift et al. (2005) predicted spherical and ellipsoidal bubble shapes.

The algebraic equation (Zwillinger, 2011) of an oblate spheroid is

$$\frac{x^2 + z^2}{a^2} + \frac{y^2}{c^2} = 1. \tag{3}$$

The inclination angle α, major semi-axis a and minor semi-axis c from each bubble were extracted from the 2D image of the bubble. Unfortunately, the general assumption for Eq. (3) is that the spheroid is not rotated and the midpoint equals the origin of the coordinate system. These assumptions did not apply to rising bubbles. Through the movement of the bubble, a translation of the midpoint and a rotation of the semi-axis occurred. Consequently, a transformation of the coordinate system was necessary to fulfill the criteria for Eq. (3).

The coordinate system was translated to the midpoint of the bubble $\boldsymbol{X_b}$ and rotated around the bubble's angle of inclination in the xy-plane to receive the coordinate system of the bubble (Fig. 8). This led to the following transformation

$$\boldsymbol{X'} = \begin{bmatrix} \cos(\alpha) & -\sin(\alpha) & 0 \\ \sin(\alpha) & \cos(\alpha) & 0 \\ 0 & 0 & 1 \end{bmatrix} \cdot \boldsymbol{X} - \boldsymbol{X_b}. \tag{4}$$

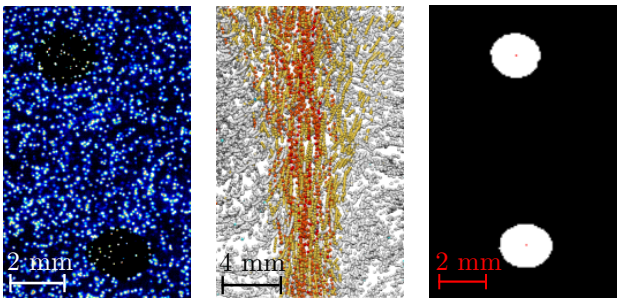

(a) (b) (c)

Figure 7: Image processing steps to calculate particle (a,b) and bubble trajectory (c). (a) Difference image after subtraction of bubble mask from original image. (b) Calculated particle trajectories with Shake-the-box algorithm for 150 time steps. (c) Extracted bubble mask where the mid points are highlighted red.

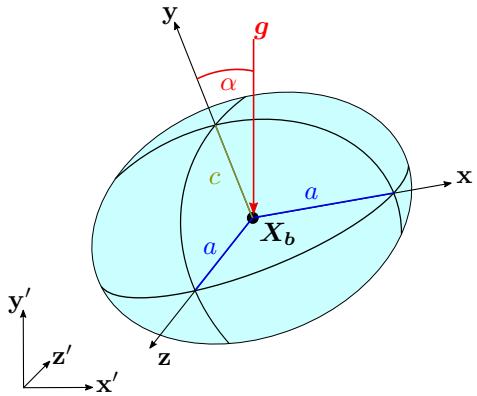

Figure 8: Definition of rotated spheroid with major axis$a$ and minor axis c, $\boldsymbol{X_b}$ the center point and inclination angle α between axis of symmetry and vector of gravitational acceleration $\boldsymbol{g}$. The illustration is within the global (x', y', z') and transformed (x, y, z) coordinate system.

Consequently, all further calculation took place within the transformed coordinate system to fulfill the criteria for Eq. (3).

3.4. Calculation of collection zone recovery based on the number of attached particles

The collection zone recovery R_c is defined as

$$R_c = \frac{n}{V \cdot c_p}, \tag{5}$$

following the the approach of Nguyen et al. (1998) which is adapted in the following to the needs of the tomo PIV. In Eq. (5), n is the number of attached particles per bubble, V the reference volume and c_p the particle concentration within the column. The reference volume in the present work comprises the actually captured rising path of a bubble as illustrated in Fig. 10b with the cylinder height given by the height H_m of the measurement volume

$$V_m = \frac{H_m(d_p + d_b)^2\pi}{4}. \tag{6}$$

The particle concentration c_p was calculated by the number of particle tracks within the measurement volume per time step. As a result, the collection zone recovery R_c is then given by

$$R_c = \frac{n}{c_p} \cdot \frac{4}{H_m(d_p + d_b)^2\pi} \tag{7}$$

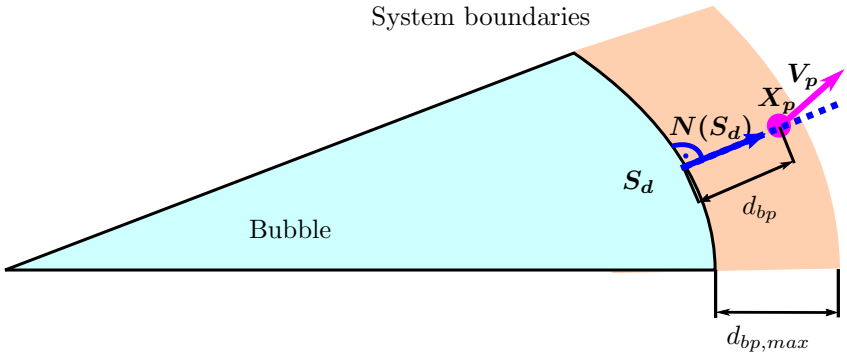

Figure 9: Description to check criterion (ii) with $d_{bp,max}$ as size of the system boundaries. Calculation of the length d_{bp} of the normal vector $\boldsymbol{N(S_d)}$ between bubble surface $\boldsymbol{S_d}$ and particle center $\boldsymbol{X_p}$.

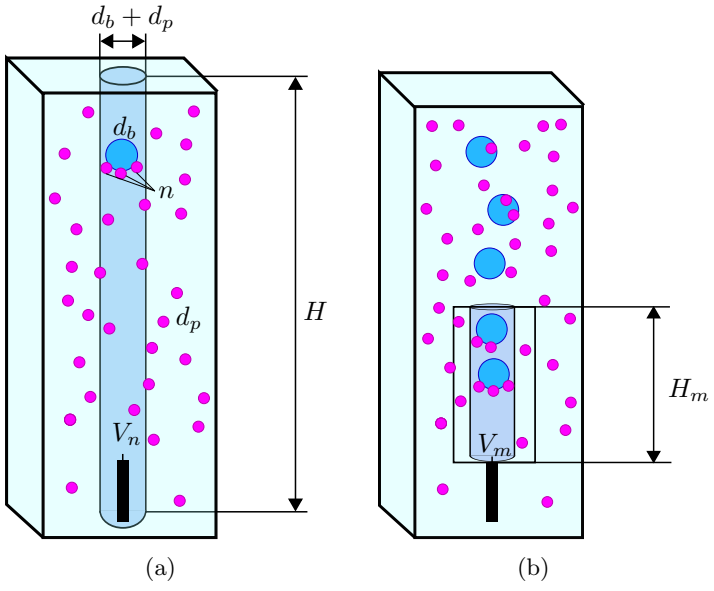

Figure 10: Definition of the cylindrical reference volume for the calculation of R_c (a) by Nguyen et al. (1998) and (b) our adaptation based on the measurement volume .

The challenge was now to determine the number of attached particle n per bubble. We defined an attached particle as a particle which remained within the near field of a bubble over a period of time. Therefore, the following conditions had to be fulfilled by the trajectory of a particle to get identified as an attached particle.

(i) The particle center is situated inside the system boundaries of the bubble.
(ii) The radial component of the particle velocity v_r in respect to the bubble velocity is below a threshold $v_{r,max}$.
(iii) The particle trajectory contains at least three track points.

The system boundary was the thin layer around the bubble surface with a maximum distance $d_{bp,max}$ to the bubble surface. Based on the definition of the reference volume as cylinder with the diameter of $d_b + d_p$, the maximum distance was defined as

$$d_{bp,max} = \frac{d_p + \sigma_S(d_b)}{2}. \tag{8}$$

The term $\sigma_S(d_b)$ accounts for the uncertainties of calculation of the bubble diameter and is based on the standard deviation σ_S of the equivalent volume diameter d_b

$$\sigma_S(d_b) = \sqrt{\frac{1}{N-1}\sum_{i=1}^{N} |d_{b,i} - \mu(d_b)|^2} \tag{9}$$

where N is the number of observations of the same bubble and $\mu(d_b)$ the mean value of d_b

$$\mu(d_b) = \frac{1}{N}\sum_{i=1}^{N} d_{b,i}. \tag{10}$$

All particle centers within $\pm d_{bp,max}$ were localized as inside, the others as outside of the system boundary. For the evaluation of the criterion (i), the distance d_{bp} between particle $\boldsymbol{X_p}$ and bubble surface $\boldsymbol{S}$ was computed.

The problem was to find the point $\boldsymbol{S_d}$ on the bubble surface which had the minimum distance to $\boldsymbol{X_p}$. Therefore, the perpendicular normal vector $\boldsymbol{N}$ on a given point on the surface $\boldsymbol{S}$ was used because the shortest line between particle and surface is oriented orthogonal to the bubble surface. The normal vector $\boldsymbol{N(S)}$ is defined as the gradient of the surface on the point $\boldsymbol{S}$ with its coordinates (s_x, s_y, s_z)

$$\boldsymbol{N} = \frac{\nabla\left(\frac{s_x^2+s_z^2}{a^2} + \frac{s_y^2}{c^2}\right)}{\left|\nabla\left(\frac{s_x^2+s_z^2}{a^2} + \frac{s_y^2}{c^2}\right)\right|} = \frac{1}{\sqrt{\frac{s_x^2+s_z^2}{a^4} + \frac{s_y^2}{c^4}}} \begin{bmatrix} \frac{s_x}{a^2} \\ \frac{s_y}{c^2} \\ \frac{s_z}{a^2} \end{bmatrix}. \tag{11}$$

Consequently, the desired normal vector $\boldsymbol{N(S_d)}$ had to point towards $\boldsymbol{X_p}$ which yield the linear equation

$$\boldsymbol{X_p} = \boldsymbol{S_d} + d_{bp} \cdot \boldsymbol{N(S_d)}. \tag{12}$$

To solve Eq. (12) and gain d_{bp}, another equation was required as this equation contained four unknown variables (s_{dx}, s_{dy}, s_{dz}, d_{bp}). Therefore, Eq. (3) was included because $\boldsymbol{S_d}$ was located on the surface of the spheroid. After solving this system of equations, the minimum distance d_{bp} between $\boldsymbol{S_d}$ and $\boldsymbol{X_p}$ was found.

Criterion (ii) compared the radial component of the relative velocity $\boldsymbol{V_r}$ between bubble and particle, yielding $\boldsymbol{V_r} = \boldsymbol{V_p} - \boldsymbol{V_b} = (u_r, v_r, w_r)^T$. In general, after a collision of a particle with a bubble, the particle slid along the bubble surface for a finite period of time (Yoon and Luttrell, 1989). Thus, a particle attachment occurred if a particle moved only tangential along the bubble surface without a radial movement in respect to the bubble velocity. Therefore, the radial velocity component of the particles were calculated based on a transformation from Cartesian (x, y, z) to spherical coordinates (r, θ, ϕ)

$$r^2 = x^2 + y^2 + z^2. \tag{13}$$

Consequently, the radial velocity component v_R was

$$v_R = \frac{\partial r}{\partial t} = \dot{r} = \frac{x u_R + y v_R + z w_R}{r}. \tag{14}$$

$$\tag{15}$$

Theoretically, criterion (ii) was fulfilled if the radial component of the particles relative velocity v_r was zero. However, through measurement uncertainties, the particle velocity could be greater than zero although an attachment occurred. Therefore, a threshold value $v_{r,max}$ as the standard deviation of the absolute value of bubble rising velocity $\sigma_s(|\boldsymbol{V_b}|)$ was used and calculated analogous to Eq. 9 and Eq. 10. Criterion (iii) was tested directly with the results of the PTV measurements.

Finally, if a particle met all three criteria, it was classified as attached. The ratio between the sum of attached particles and the number of bubbles equaled to n, the number of attached particles per bubble. Subsequently, the collection zone recovery was calculated by Eq. (7).

4. Results

4.1. Visualization of the fluid flow within the measurement volume

Turbulence plays an important role in the flotation process. It influences the transport of solids, particle-bubble collisions, attachment, and detachment. Thus, it has a major impact on the recovery. Therefore, the measurement of the turbulent flow field within a flotation cell gives important information concerning the recovery rate.

Using the neutrally buoyant PS particles, PTV can measure the recovery and simultaneously the flow field. One example is shown in Fig. 11. This figure illustrates the vorticity and velocity of the liquid flow within the measurement volume for one time step. The arrows label the velocity with a color code for the absolute value. The background shows the vorticity in z-direction. The bubble is released at point (-3 mm, -10 mm) and rises in a zig-zag motion in positive y-direction. The flow field can be divided into two areas based on the velocity and vorticity. The first area is classified between the gas outlet and $y = 5$ mm. After the gas release, the vorticity is concentrated within the bubble wake, where the absolute values of vorticity and maximum velocities are higher than in the second area. Above $y = 5$ mm, the velocity field widens and velocity gradients decrease.

Clift et al. (2005) compared the flow of a rising spherical and ellipsoidal bubble with the flow around a sphere. For a flow with $Re = 484$, ring vortices are shedded periodically behind the bubble. A vortex ring breaks away from the bubble and drifts downstream in the wake flow until it diffuses. For lower Re numbers the ring vortex remains behind the bubble and just oscillates back and forth in position with time. After the release of the bubble from the needle, the bubble accelerates until it reaches its terminal velocity which leads also to an increase of Re from 0 to 484. Therefore, a single ring vortex remains in the wake of bubble as seen in the first area ($y < 5$ mm). In the second area, the terminal velocity of the bubble is reached, subsequently the periodically shedding of vortex rings starts and causes a zig-zag motion of the bubble (Clift et al., 2005). Both effects favor a mixing of the liquid phase so that the movement of the liquid flow extends its area and the velocity range is more balanced.

4.2. Interaction between bubble and particles

The recovery is a quantitative measure of the interaction between particles and bubbles. Fig. 13 illustrates an example of an attached particle which is captured and detected by our method. In Fig. 12, particles within a maximum distance of half of the major semi-axis of the bubble, $\frac{a}{2}$, are shown. Colors indicate if a particle was attached to the bubble. For the visualization, the bubble shape is averaged over time.

It is obvious that the majority of particles undergoes collision and attachment at the trailing edge of the bubble. These findings are in contrast to the literature (e.g. Yoon and Luttrell, 1989; Nguyen et al., 1998) where predominantly attachment processes are analyzed following a collision of a particle at the leading edge of the bubble and a subsequent sliding along the bubble surface. The reason is seen in the smaller density of

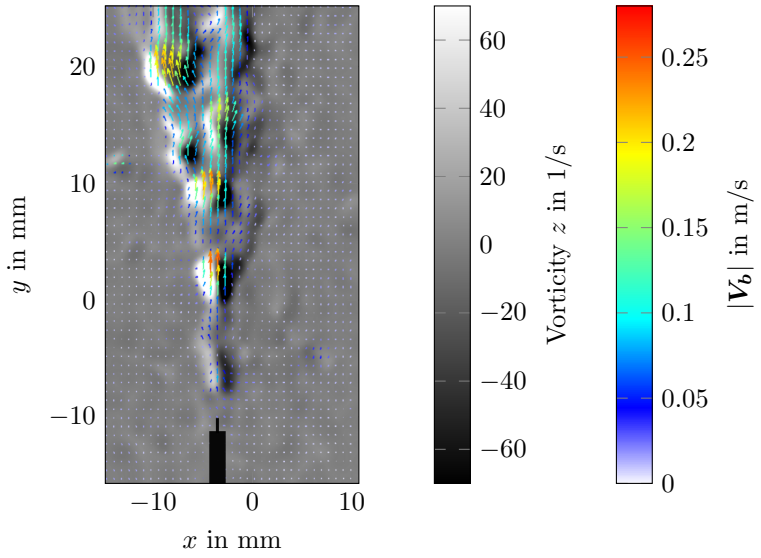

Figure 11: Velocity and vorticity field within bubble column for one time step. (Particle system PS33, $Re = 484$.)

the used PS particles compared to that of the rather heavy mineral particles. The mineral particles have a higher inertia and deviated from the streamlines already at low accelerations of the flow to collide with the top of the bubble. In contrast, our neutrally buoyant particles are expected to follow the streamlines during a low acceleration of the flow. However, at the trailing edge of the bubble higher accelerations could occur through the vortices in the bubble wake (Fig. 11). Due to their inertia, the particles trajectories deviated from the streamlines and collided with the bubble surface. A three-phase contact line could form and the particle was attached to the bubble.

4.3. Comparison of measured and modeled collection zone recovery in dependence on the particle diameter

One aim of the development of our novel method is to measure the collection zone recovery and to verify existing recovery models. Therefore, Fig. 14 compares the measured recovery with the calculated recovery, R_c,

$$R_c = 1 - \exp\left[-P_c P_a (1 - P_d)\left(1 + \frac{v_s}{|\boldsymbol{V_b}|}\right)\right] \tag{16}$$

based on the model of Nguyen et al. (1998) depending on the particle diameter. In Eq. (16), P_c, P_a and P_d refer to the probabilities of collision, attachment and detachment, respectively. The settling velocity v_s was estimated by Kürten et al. (1966)

$$v_s = \frac{1}{18} \cdot \frac{d_p^2 \cdot (\rho_p - \rho_l)}{\rho_l \cdot \nu} \tag{17}$$

with the particle density ρ_p, the liquid density ρ_l and the kinematic viscosity ν. In the case of fine and inertialess particles, Nguyen et al. (1998) predicted P_c as

$$P_c = \frac{2|\boldsymbol{V_b}|D}{9(|\boldsymbol{V_b}| + v_s)Y}\left(\frac{d_p}{d_b}\right)^2\left[\sqrt{(X+C)^2 + 3Y^2} + 2(X+C)\right]^2 \tag{18}$$

with X,Y,C and D as dimensionless number depending on Re, d_p, d_b, $|\boldsymbol{V_b}|$ and v_s and defined in Nguyen et al. (1998). The other probabilities were assumed as follows. The probability of attachment refers to the possibility of the rupture of the liquid film between bubble and particle and the formation of a three-phase contact line. This formation takes place on a nanometer scale and can not be observed with our method. Therefore, we assumed all collisions led to attachment, $P_a = 1$, and no detachment occurred, $P_d = 0$.

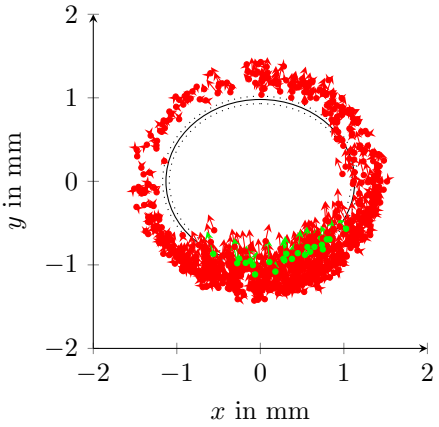

Figure 12: Accumulation of all particle trajectories within a maximum distance 0.5 mm to one bubble over 1000 time steps. The shape of the bubble is displayed as a continuous line. The dotted line marks the maximum search distance $d_{b,max}$ for criterion (ii). The particle trajectory is colored green, if particle attached to bubble and red, if no attachment occurred. (Particle system PS33, $n = 0.46$ particle/bubble, $v_{r,max} = 0.03$ m/s, $d_{b,max} = 0.0415$ mm.)

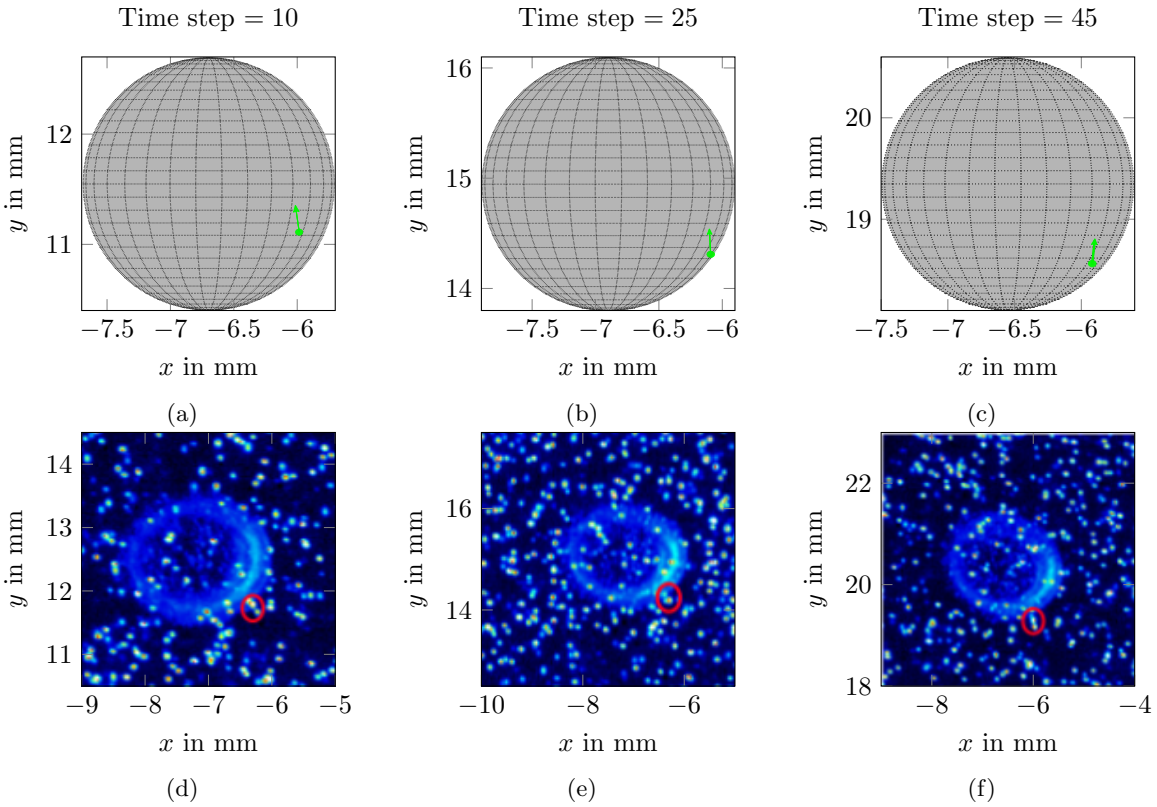

Figure 13: Image sequence of a particle attached to a bubble over time. (a-c) Measured trajectory of attached particle (see green dot). (d-f) Captured image of particle trajectory. There is an uncertainty of the coordinates between 2D image and 3D trajectory caused by image distortion. Particle system PS33.

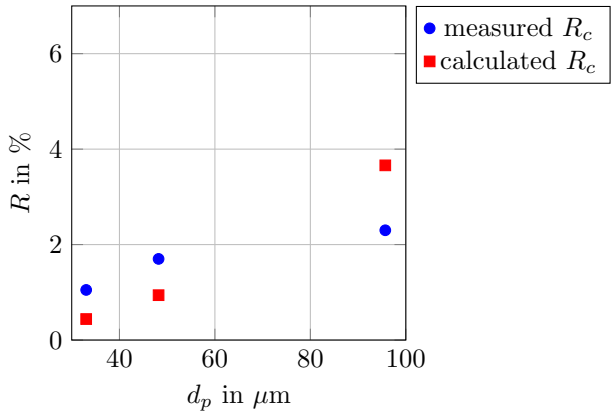

Figure 14: Comparison of collection zone recovery based on a calculation with the model of Nguyen et al. (1998) and measured with our method.

Fig. 14 shows a rise of R_c with an increase of d_p for both methods. The difference between the measured and modeled value of R_c varies with the particle diameter. For smaller particle diameter ($d_p = 33.03, 48.2\ \mu$m), the measured collection recovery is in approximately by a factor of 2.1 larger as the modeled R_c, whereas at a coarser particle diameter ($d_p = 95.07\ \mu$m) the measured collection recovery is is approx. 0.6 of the modeled R_c.

5. Discussion and Conclusion

The method presented a modification of 4D-PTV. The traditional application for PTV is the tracking of individual tracer particles over time. Usually, the particles are neutrally buoyant and very small, in water typically below 10 μm. Thus, they follow the fluid motion nearly perfectly. However, such particles would not collide with the bubble, since they are displaced by the bubble, together with the surrounding fluid. Therefore, we modified this approach by applying larger PS particles in order to mimic ore particles in a flotation cell. Similar to ore, our PS particles were hydrophobized. The larger PS particles did not follow the fluid perfectly, but collided with the bubble. For the applied particles, any velocity deficit relaxed on a time scale of $0.2 \ldots 2$ ms. The large scale flow around the rising bubble accelerated on a larger time scale of $d_B/V_B \approx 10$ ms. Therefore, our particles could follow this flow and did not collide with the leading edge of the bubble. In the wake, eddies occurred, showing smaller acceleration time scales and additionally centrifugal forces. Consequently, our particles did not perfectly follow the flow in the wake and collided with the trailing edge of the bubble. Nevertheless, they followed the flow in the wake to some extent, allowing for a rough evaluation of the vorticity and velocity in the wake. An even better representation of the mineral flotation process would be the application of fluorescent ore particles with a reasonable density and diameter, which is planned in future works. But in that case, the flow measurement will be much more unreliable.

Concerning the quantitative comparison between the measured recovery and the model by Nguyen et al. (1998) in Fig. 14 one has to consider the measurement limitations of our technique. Firstly, reflections on the bubble and overlapping particle could lead to a falsely ending particle track. Therefore, particle tracks especially close to the bubble surface were not fully coherent and might contribute two or three times to the recovery rate. This effect might artificially increase the measured recovery. Secondly, some regions behind the bubble are not covered by the cameras as seen by a lower particle density in Fig. 12 at $x < 0$. In these regions, attached particles were not recognized, decreasing the measured recovery roughly. On the other hand, the model by Nguyen et al. (1998) is not exact. For example, it neglects detachment. Since detachment is more likely for larger particles, it would significantly decrease the recovery values for the 100 μm particles. Consequently, the recovery data in Fig. 14 might be imprecise. However, it shows, that the recovery rate and the influence of the particle size is roughly reproduced by our novel measurement technique.

Another technique to measure the Lagrangian particle trajectories in the 3D space is the Positron Emission Particle Tracking (PEPT) (Parker et al., 1993). The main advantages of this method is the applicability to opaque fluids and froth and the unambiguous tracking of radioactively marked particles (Waters et al., 2008). Therefore, Boucher et al. (2017) applied this technique to a lab-scale flotation cell to track particle trajectories from hematite and quartz. On the downside, PEPT can handle only a small number of seeding particles (Barigou, 2004; Langford et al., 2016) and offers lower temporal and spatial resolution (Barigou, 2004). Therefore, PTV might be more suitable to measure the particle trajectory fields in the vicinity of a bubble with high temporal (1000 fps) and spatial (0.03 mm/px) resolution and quantify the interaction between particles and bubbles. In contrast, PEPT can follow individual particles all the way through a flotation cell and addresses the overall recovery. Combining both techniques might yield interesting insights into the relation between adsorption and recovery.

6. Acknowledgements

We thank our colleagues from NetFlot (KIC RawMaterials project no. 15062, infrastructure network "Modelling of flotation processes") for valuable discussions.

References

Anfruns, J., Kitchener, J., 1977. Rate of capture of small particles in flotation. Trans. Inst. Min. Metall. Sect. C 86, C9C15.

Atherton, T., Kerbyson, D., 1999. Size invariant circle detection. Image and Vision Computing 17, 795–803. doi:10.1016/s0262-8856(98)00160-7.

Barigou, M., 2004. Particle tracking in opaque mixing systems: An overview of the capabilities of PET and PEPT. Chemical Engineering Research and Design 82, 1258–1267. doi:10.1205/cerd.82.9.1258.44160.

Boucher, D., Jordens, A., Sovechles, J., Langlois, R., Leadbeater, T.W., Rowson, N.A., Cilliers, J.J., Waters, K.E., 2017. Direct mineral tracer activation in positron emission particle tracking of a flotation cell. Minerals Engineering 100, 155–165. doi:10.1016/j.mineng.2016.10.022.

Clift, R., Grace, J., Weber, M.E., 2005. Bubbles, Drops, and Particles. Dover Publications, Inc.

Elsinga, G.E., Scarano, F., Wieneke, B., van Oudheusden, B.W., 2006. Tomographic particle image velocimetry. Experiments in Fluids 41, 933–947. doi:10.1007/s00348-006-0212-z.

Falutsu, M., Dobby, G., 1989. Direct measurement of froth drop back and collection zone recovery in a laboratory flotation column. Minerals Engineering 2, 377–386. doi:10.1016/0892-6875(89)90006-x.

Fraunholcz, N., 1997. Plastics flotation. Ph.D. thesis. TU Delft Faculty Civil Engineering and Geosciences.

Hewitt, D., Fornasiero, D., Ralston, J., 1995. Bubble–particle attachment. J. Chem. Soc., Faraday Trans. 91, 1997–2001. doi:10.1039/ft9959101997.

Kürten, H., Raasch, J., Rumpf, H., 1966. Beschleunigung eines kugelförmigen Feststoffteilchens im Strömungsfeld konstanter Geschwindigkeit. Chem.-Ing.-Tech. 38, 941–948.

Langford, S., Wiggins, C., Tenpenny, D., Ruggles, A., 2016. Positron emission particle tracking (PEPT) for fluid flow measurements. Nuclear Engineering and Design 302, 81–89. doi:10.1016/j.nucengdes.2016.01.017.

Lindken, R., Merzkirch, W., 2002. A novel PIV technique for measurements in multiphase flows and its application to two-phase bubbly flows. Experiments in Fluids 33, 814–825. doi:10.1007/s00348-002-0500-1.

Maas, H.G., 1996. Contributions of digital photogrammetry to 3-d PTV, in: Three-Dimensional Velocity and Vorticity Measuring and Image Analysis Techniques. Springer Netherlands. ERCOFTAC Series, pp. 191–207. doi:10.1007/978-94-015-8727-3_9.

Maas, H.G., Gruen, A., Papantoniou, D., 1993. Particle tracking velocimetry in three-dimensional flows. Experiments in Fluids 15, 133–146. doi:10.1007/bf00190953.

Moys, M., Yianatos, J., Larenas, J., 2010. Measurement of particle loading on bubbles in the flotation process. Minerals Engineering 23, 131–136. doi:10.1016/j.mineng.2009.11.004.

Nguyen, A., Schulze, H.J., 2003. 118: Colloidal Science of Flotation (Surfactant Science). volume 118. CRC Press.

Nguyen, A.V., Ralston, J., Schulze, H.J., 1998. On modelling of bubble–particle attachment probability in flotation. International Journal of Mineral Processing 53, 225–249. doi:10.1016/s0301-7516(97)00073-2.

Parker, D., Broadbent, C., Fowles, P., Hawkesworth, M., McNeil, P., 1993. Positron emission particle tracking - a technique for studying flow within engineering equipment. Nuclear Instruments and Methods in Physics Research Section A: Accelerators, Spectrometers, Detectors and Associated Equipment 326, 592–607. doi:10.1016/0168-9002(93)90864-e.

Pascoe, R., 2005. The use of selective depressants for the separation of ABS and HIPS by froth flotation. Minerals Engineering 18, 233–237. doi:10.1016/j.mineng.2004.07.006.

Ralston, J., Fornasiero, D., Hayes, R., 1999. Bubble–particle attachment and detachment in flotation. International Journal of Mineral Processing 56, 133–164. doi:10.1016/s0301-7516(98)00046-5.

Scarano, F., 2012. Tomographic PIV: principles and practice. Measurement Science and Technology 24, 012001. doi:10.1088/0957-0233/24/1/012001.

Schanz, D., Gesemann, S., Schrder, A., 2016. Shake-the-box: Lagrangian particle tracking at high particle image densities. Experiments in Fluids 57, 70. doi:10.1007/s00348-016-2157-1.

Schubert, H., 1999. On the turbulence-controlled microprocesses in flotation machines. International Journal of Mineral Processing 56, 257–276. doi:10.1016/s0301-7516(98)00048-9.

Seaman, D., Franzidis, J.P., Manlapig, E., 2004. Bubble load measurement in the pulp zone of industrial flotation machines—a new device for determining the froth recovery of attached particles. International Journal of Mineral Processing 74, 1–13. doi:10.1016/j.minpro.2004.04.001. wOS:000224927600001.

Sharma, A., Ruckenstein, E., 1990. Energetic criteria for the breakup of liquid films on nonwetting solid surfaces. Journal of Colloid and Interface Science 137, 433–445. doi:10.1016/0021-9797(90)90418-n.

Sutherland, K.L., 1948. Physical chemistry of flotation. XI. kinetics of the flotation process. The Journal of Physical and Colloid Chemistry 52, 394–425. doi:10.1021/j150458a013.

Wang, C., Wang, H., Gu, G., Lin, Q., Zhang, L., Huang, L., Zhao, J., 2016. Ammonia modification for flotation separation of polycarbonate and polystyrene waste plastics. Waste Management 51, 13–18. doi:10.1016/j.wasman.2016.02.037.

Waters, K., Rowson, N., Fan, X., Parker, D., Cilliers, J., 2008. Positron emission particle tracking as a method to map the movement of particles in the pulp and froth phases. Minerals Engineering 21, 877–882. doi:10.1016/j.mineng.2008.02.007.

Wieneke, B., 2008. Volume self-calibration for 3d particle image velocimetry. Experiments in Fluids 45, 549–556. doi:10.1007/s00348-008-0521-5.

Wieneke, B., 2012. Iterative reconstruction of volumetric particle distribution. Measurement Science and Technology 24, 024008. doi:10.1088/0957-0233/24/2/024008.

Yoon, R.H., 2000. The role of hydrodynamic and surface forces in bubble–particle interaction. International Journal of Mineral Processing 58, 129–143. doi:10.1016/s0301-7516(99)00071-x.

Yoon, R.H., Luttrell, G.H., 1989. The effect of bubble size on fine particle flotation. Mineral Processing and Extractive Metallurgy Review 5, 101–122. doi:10.1080/08827508908952646.

Yoon, R.H., Soni, G., Huang, K., Park, S., Pan, L., 2016. Development of a turbulent flotation model from first principles and its validation. International Journal of Mineral Processing 156, 43–51. doi:10.1016/j.minpro.2016.05.009.

Yuen, H.K., Princen, J., Dlingworth, J., Kittler, J., 1989. A comparative study of hough transform methods for circle finding, in: Procedings of the Alvey Vision Conference 1989, Alvey Vision Club. pp. 29.1–29.6. doi:10.5244/c.3.29.

Ziegenhein, T., Lucas, D., 2016. On sampling bias in multiphase flows: Particle image velocimetry in bubbly flows. Flow Measurement and Instrumentation 48, 36–41. doi:10.1016/j.flowmeasinst.2016.02.003.

Zwillinger, D., 2011. CRC Standard Mathematical Tables and Formulae. CRC press.